Journal of the Earth and Space Physics, Vol. 45, No. 4, Winter 2020, P. 15-25
DOI: 10.22059/jesphys.2019.256185.1006999

Center of Mass Estimation of Simple Shaped Magnetic Bodies Using Eigenvectors of Computed Magnetic Gradient Tensor

Karimi, K.[1*], Shirzaditabar, F.[2], Amirian, A.[3] and Mansoobi, A.[1]

1. M.Sc. Graduated, Department of Physics, Faculty of Sciences, Razi University, Kermanshah, Iran
2. Assistant Professor, Department of Physics, Faculty of Sciences, Razi University, Kermanshah, Iran
3. Ph.D. Student, Department of Earth & Planetary Sciences, Macquarie University, Sydney, NSW

(Received: 28 April 2018, Accepted: 1 Jan2019)

Abstract
Computed Magnetic Gradient Tensor (CMGT) includes the first derivatives of three components of magnetic field of a body. At the eigenvector analysis of Gravity Gradient Tensors (GGT) for a line of poles and point pole, the eigenvectors of the largest eigenvalues (first eigenvectors) point precisely toward the Center of Mass (COM) of a body. However, due to the nature of the magnetic field, it is shown that these eigenvectors for the similar shaped magnetic bodies (line of dipoles and point-dipole), in CMGT, are not convergent to COM anymore. Rather, in the best condition, when there is no remanent magnetization and the body is in the magnetic poles, their directions are a function of data point locations. In this study, by reduction to the pole (RTP) transformation and calculation of CMGT, a point is estimated that its horizontal components are exactly the horizontal components of the COM and its vertical component is a fraction of the COM vertical component. These obtained depth values are 0.56 and 0.74 of COM vertical components for a line of dipoles and point-dipole, respectively. To reduce the turbulent effects of noise, "Moving Twenty five Point Averaging" method and upward continuation filter are used. The method is tested on solitary and binary simulated data for bodies with varying physical characteristics, inclinations and declinations. Finally, it is imposed on two real underground examples; an urban gas pipe and a roughly spherical orebody and the results confirm the methodology of this syudy.

Keywords: Computed Magnetic Gradient Tensor, Center of Mass, First Eigenvectors.

1. Introduction
Magnetic and Gravity gradient tensors (MGT and GGT) contain the second derivatives of the earth magnetic and gravitational potentials in three directions, respectively. The history of Gravity gradiometry goes back to 1886, when the petroleum industry was revolutionized by Baron von Eötvös' invention (Bell and Hansen, 1998). However, the annals of employing MGT are much shorter. In 1972, Frahm used MGT data with an explicit solution to a point-by-point magnetic dipole localization. Reford and Sumner (1964) gave an account of equipment, survey techniques, data reduction and interpretational methods regarding airborne surveys in mining and petroleum exploration, geological mapping, and crustal and upper mantle studies. Reid et al. (1990) interpreted the magnetic data by deconvolution using Euler's homogeneity relation. Their method, employing gradients of magnetic field, was remarkably accurate in detection of some bodies like dikes, vertical pipes and contacts, and also, it was independent of remanence. In the last two decades, various techniques of MGT data have been widely improved (Schmidt and Clark, 2000; Schmidt and Bracken, 2004; Gamey et al., 2004; Doll et al., 2006; Chianese and Lapenna, 2007). Pedersen and Rasmussen (1990) showed that using MGT and GGT data is functional for geophysical prospecting. They discussed in detail the practical problems encountered in the collecting and processing of the MGT and introduced scalar invariants to indicate dimensionality of the sources. They also showed that the maximum eigenvalues and their corresponding eigenvectors (first eigenvectors) of the GGT are related to the COM of simple sources; however, they did not analyze the properties of these eigenvectors for simple magnetic bodies because they did not show organized or obvious orientations. Chianese and Lapenna (2007) introduced a new tomographic technique for magnetic data inversion in near-surface geophysical investigations

*Corresponding author: kuroshkarimi88@gmail.com

conducted in environmental and engineering applications. Their method was based on cross-correlation integral between measured and theoretically produced magnetic fields. At the same year, Shaw et al. (2007) could compute the depths of four idealized magnetic sources by the Walsh spectra of the total-field magnetic anomalies. These sources were a monopole, a line of monopoles, a dipole and a line of dipoles. Three years later, Oruc (2010) proposed a method using ratio of analytic signal of magnetic field and its MGT components for simple causative bodies to estimate their locations. Beiki and Pedersen (2010) located the causative bodies from a collection of eigenvectors of the GGT using robust least squares procedure. In a parallel way, one year later, they employed pseudogravity gradient tensor (PGGT) to detect dimensionality, strike direction and location of geological bodies, simultaneously having both magnetic and gravitational properties (Beiki and Pedersen, 2011). Finally, Eppelbaum (2015) presented a quantitative magnetic anomalies interpretation approximated by thick bed models. He reasonably argued that many geological targets resemble thick beds, thin horizontal plates and intermediate forms lying between those two models. Using this quality, his method yielded acceptable results.

In this paper, with the aid of least squares procedure for a collection of first eigenvectors of CMGT, the location of simple causative bodies (line of dipoles and point dipole) are approximated with an acceptable accuracy. The concept of point-dipole and line of dipoles is often employed in the analysis of magnetic anomalies caused by geologic bodies whose geometric shapes approach those of: 1) spheres and 2) thin horizontal cylinder or narrow prisms of finite depth extent, respectively. Magnetic anomalies observed in archaeological prospecting may be classified roughly in two categories: the ones that correspond to elongate features (ditches and buried cylindrical graves for example), and those that have limited lateral extension in both directions. For the first category, a line of dipoles must be used rather than one dipole alone, which is convenient for the second category. Because of using the derivatives of magnetic field components, "Moving Twenty five Point Averaging" and upward continuation methods are employed to decrease the disruptive impact of noise on the data.

2. Theory

In order to calculate COM of a line of dipoles and a point dipole, their measured magnetic fields are reduced to the pole, and the derivatives of their three components (Bx, B_y, B_z), using Fourier Domain, in three orthogonal directions are calculated (Blakely, 1996). Then, for each data point, a 3×3 matrix, containing these derivatives (CMGT) is constituted:

$$\mathbf{\Gamma} = \mathbf{CMGT} = \begin{bmatrix} B_{xx} & B_{xy} & B_{xz} \\ B_{yx} & B_{yy} & B_{yz} \\ B_{zx} & B_{zy} & B_{zz} \end{bmatrix} \quad (1)$$

Since the above tensor is symmetrical, its eigenvalues (b_i) are real and eigenvectors ($\mathbf{v}_i$) are perpendicular. Therefore, the following relation holds:

$$\mathbf{\Gamma v_i} = b_i \mathbf{v_i} \quad (2)$$

For a line of dipoles along **y** axis and depth of "Z_0" in the magnetic poles, without remanent magnetization, $\mathbf{\Gamma}$ is (Pedersen and Rasmussen, 1990):

$$\mathbf{\Gamma}_{CYL} = \frac{-2M}{R^3}\begin{pmatrix} -2c+8a^2c & -2a+8ac^2 \\ -2a+8ac^2 & -6b+8c^3 \end{pmatrix} = \begin{pmatrix} \Gamma_{11} & \Gamma_{12} \\ \Gamma_{12} & \Gamma_{22} \end{pmatrix} \quad (3)$$

where "M" is the magnetization of a line of dipoles, $a = \frac{(x-x_0)}{R}$, $c = -\frac{z_0}{R}$ and $R = |\mathbf{r} - \mathbf{r}_0| = [(x-x_0)^2 + z_0^2]^{(\frac{1}{2})}$ For such a matrix, the eigenvalues are: $\lambda_1 = +\frac{4M}{R^3}$ and $\lambda_2 = -\frac{4M}{R^3}$ (Pedersen and Rasmussen, 1990). The eigenvector corresponding to the larger eigenvalue (i.e. first eigenvector) is:

$$\mathbf{v}_1 = \frac{1}{\sqrt{1+\alpha^2}}\begin{pmatrix} \alpha \\ 1 \end{pmatrix} \quad (4)$$

where $\alpha = \frac{\Gamma_{12}}{\lambda_1 - \Gamma_{11}}$.

Eventually, the angle between the first eigenvectors and z axis at data point locations which is a function of x (this axis is perpendicular to the strike direction), can be written as:

$$\Theta(x) = \tan^{-1}(\alpha) = \left[\tan^{-1}\left(\frac{\Gamma_{12}}{\lambda_1 - \Gamma_{11}}\right) \right] \quad (5)$$

In a counter clockwise rotation, Θ has positive values. Figure 1(a) illustrates the schematic image of magnetic source along a profile, the directions of the first eigenvectors and other features. Figure 1(b) demonstrates "Θ" pertaining to a line of dipoles lain at (100 m, 100 m, 40 m). It is evident that a number of first eigenvectors incline to the causative body, but towards the ends of the profile (x ≤ 31 m and x ≥169 m), they deviate completely from the magnetic source.

Similarly, for a point dipole with depth of "Z_0" in the magnetic poles without remanent magnetization, **Γ** is (Pedersen and Rasmussen, 1990):

$$\Gamma_{SPHERE} = -M\frac{3}{R^4}\begin{pmatrix} -c+5a^2c & 5abc & -a+5ac^2 \\ 5abc & -c+5b^2c & -b+5bc^2 \\ -a+5ac^2 & -b+5bc^2 & -3c+5c^3 \end{pmatrix} = \begin{pmatrix} \Gamma_{11} & \Gamma_{12} & \Gamma_{13} \\ \Gamma_{12} & \Gamma_{22} & \Gamma_{23} \\ \Gamma_{13} & \Gamma_{23} & \Gamma_{33} \end{pmatrix} \quad (6)$$

in which "M" is the magnetization of a point dipole, and $a = \frac{(x-x_0)}{R}$, $b = \frac{y-y_0}{R}$ and $c = -\frac{z_0}{R}$. Three eigenvectors of $\mathbf{\Gamma}_{SPHER}$ are calculated as:

$$\begin{cases} \lambda_1 = C + D \\ \lambda_2 = -\frac{C+D}{2} + \frac{C-D}{2}\sqrt{-3} \\ \lambda_3 = -\frac{C+D}{2} - \frac{C-D}{2}\sqrt{-3} \end{cases} \quad (7)$$

where $C = \left\{\frac{I_2}{2} + \left[\left(\frac{I_2}{2}\right)^2 + \left(\frac{I_1}{3}\right)^3\right]^{\left(\frac{1}{2}\right)}\right\}^{\frac{1}{3}}$,

$D = \left\{\frac{I_2}{2} - \left[\left(\frac{I_2}{2}\right)^2 + \left(\frac{I_1}{3}\right)^3\right]^{\left(\frac{1}{2}\right)}\right\}^{\frac{1}{3}}$, $I_1 = \frac{-9M^2(1+2c^2)}{r^8}$ and $I_2 = \frac{-27M^3c(1+c^2)}{r^{12}}$ (Pedersen and Rasmussen, 1990).

The first eigenvector (i.e. the eigenvector corresponding to the largest eigenvalue, λ_1) is derived as follows:

$$\mathbf{V}_1 = \frac{1}{\sqrt{\alpha^2 + \beta^2 + 1}}\begin{pmatrix} \alpha \\ \beta \\ 1 \end{pmatrix} \quad (8)$$

Where

$$\alpha = \frac{\beta + \Gamma_{13}}{\lambda_1 - \Gamma_{11}} \quad \text{and} \quad \beta = -\frac{\Gamma_{12}(\Gamma_{33} - \lambda_1) - \Gamma_{13}\Gamma_{22}}{\Gamma_{13}(\lambda_1 - \Gamma_{22}) + \Gamma_{12}\Gamma_{23}}$$

For a profile passing over the sphere COM and parallel to x axis ($y=y_0$), some of the components of **Γ** are zero. Then we have:

$$\mathbf{\Gamma} = \begin{pmatrix} \Gamma_{11} & 0 & \Gamma_{13} \\ 0 & \Gamma_{22} & 0 \\ \Gamma_{13} & 0 & \Gamma_{33} \end{pmatrix}, \quad \beta = 0 \quad \text{and} \quad \alpha = \frac{\Gamma_{13}}{\lambda_1 - \Gamma_{11}}.$$

Hence, Θ is obtained by the following equation:

$$[\Theta(x)]_{y=y_0} = \tan^{-1}(\alpha) = \left[\tan^{-1}\left(\frac{\Gamma_{13}}{\lambda_1 - \Gamma_{11}}\right) \right] \quad (9)$$

The trend of this function on a profile line passing over the dipole, lain at (100 m, 100 m, 40 m), is similar to that of a line of dipoles (see Figure 1(c)).

The first eigenvector, "$\mathbf{v}_{1,i}$" at the i^{th} data point, approximately aims for a point surrounding the underground causative body called "Q_0". This vector passing through each data point creates a distance with Q_0 (Figure 1(a)). This distance is (Beiki and Pedersen, 2010):

$$\Delta\delta_i = \left|\mathbf{v}_{1,i} \times (\mathbf{r}_0 - \mathbf{r}_i)\right| \quad (10)$$

where

$$v_{1,i} = \frac{1}{\left|\boldsymbol{r}_i - \boldsymbol{r}_0'\right|}\left[x_i - x'_{i,0}, y_i - y'_{i,0}, z_i - z'_{i,0}\right]$$

in which

$$\left|\boldsymbol{r}_i - \boldsymbol{r}_0'\right| = \sqrt{(x_i - x'_{i,0})^2 + (y_i - y'_{i,0})^2 + (z_i - z'_{i,0})^2}.$$

$\boldsymbol{r_0}$ and $\boldsymbol{r_i}$ are the coordinates of Q_0 and i^{th} data point, respectively. $\boldsymbol{r'_0}$ is a point along "$\mathbf{v}_{1,i}$"

that creates the distance $\Delta\delta_i$ with $\boldsymbol{r_0}$. The square distances of "$\Delta\delta_i$"s for a group of first eigenvectors can be expressed as:

$$D = \sum_{i=1}^{N} \left(\Delta\delta_i\right)^2 \tag{11}$$

where N is the number of data points inside any selected window. By minimizing Equation (11), the location of point "$\mathbf{Q_0}$"is obtained (modified from Menke, 2012).

$$\mathbf{Q_0^{est}} = \left(\mathbf{G}^T\mathbf{G}\right)^{-1}\mathbf{G}^T\mathbf{d} \tag{12}$$

In Equation (12), we have:

$$\mathbf{G} = \begin{bmatrix} \mathbf{G_1} \\ \mathbf{G_2} \\ . \\ . \\ . \\ \mathbf{G_N} \end{bmatrix}, \qquad \mathbf{d} = \begin{bmatrix} \mathbf{d_1} \\ \mathbf{d_2} \\ . \\ . \\ . \\ \mathbf{d}_N \end{bmatrix},$$

$$\mathbf{d_i} = \mathbf{G_i r_i} = \begin{bmatrix} 0 & -\mathbf{v}_{z,i} & \mathbf{v}_{y,i} \\ \mathbf{v}_{z,i} & 0 & -\mathbf{v}_{x,i} \\ -\mathbf{v}_{y,i} & \mathbf{v}_{z,i} & 0 \end{bmatrix} \begin{bmatrix} \mathbf{x_i} \\ \mathbf{y_i} \\ \mathbf{z_i} \end{bmatrix}$$

The covariance matrix of the Equation (12) is given by (modified from Menke, 2012):

$$\operatorname{cov} Q_0^{est} = \begin{bmatrix} c_{11} & c_{12} & c_{13} \\ c_{21} & c_{22} & c_{23} \\ c_{31} & c_{32} & c_{33} \end{bmatrix} \tag{13}$$

In Equation (13), $c_{11}, c_{22}, \mathrm{c}_{33}$ are variances (uncertainties) along **x**, **y** and **z** axes, in turn. Finally, the standard error is calculated from the following relation:

$$s = \sqrt{c_{11} + c_{22} + \mathrm{c}_{33}} \longrightarrow S_{normalized} = \frac{S}{Z_0} \tag{14}$$

where "Z_0" is the depth component of the estimated location of "$\mathbf{Q_0}$".

3. Work flow

In the magnetic poles, the maximum or minimum value of the first vertical derivative of the vertical component of magnetic field, B_{zz}, lies approximately over the center of mass for positive and negative anomalies, respectively (Beiki and Pedersen, 2010). To find the maximum or minimum point in the case in which it occurs among four data points in a grid map, we can use the method introduced by Blakely and Simpson (1986). Then, a window with a center at maximum of B_{zz} is considered. We change the size of the window around the same center until the standard error reaches to the minimum value (notice that in the case of a line of dipoles, the window can lie anywhere on the linear B_{zz} maximum except the edges). The obtained solution with the minimum standard error (MSE) is the most reliable one. After running the present algorithm on many of synthetic spherical and cylindrical models, we empirically obtained that the calculated vertical component of the point "Q_0", i.e. "Z_0", is a fraction of vertical component of COM (Z_{COM}). And the estimated horizontal location of Q_0, is the same as those of COM. The relation between the estimated location of Q_0 and COM are as follows:

For a point-dipole: $(X_0, Z_0) = (X_{COM}, 0.74\times Z_{COM})$

For a line of dipoles: $(X_0, Y_0, Z_0) = (X_{COM}, Y_{COM}, 0.56\times Z_{COM})$.

The resulted fraction of each type of simulated model, with varying depth and size, is almost the same.

4. Synthetic models

In this section, firstly, two sets of synthetic models in absence and presence of noise are tested. They are isolated line of dipoles (horizontal cylinders "A" and "B") and isolated point-dipoles (spheres "A" and "B"). Then, we go further and examine two close parallel lines of dipoles in a virtually lateral neighborhood (cylinders "C" and "D"). Thereafter, two close point-dipoles in an almost lateral neighborhood (spheres "C" and "D"), and finally, two neighboring point-dipoles in an absolutely vertical neighborhood (spheres "E" and "F") are employed to see the impression of interfering sources on solutions (see Figures 3(a), (b) and (c)). The characteristics of models are given in Table 1. The areas of interest and cell sizes are 205×205 m^2 and 5×5 m^2, respectively.

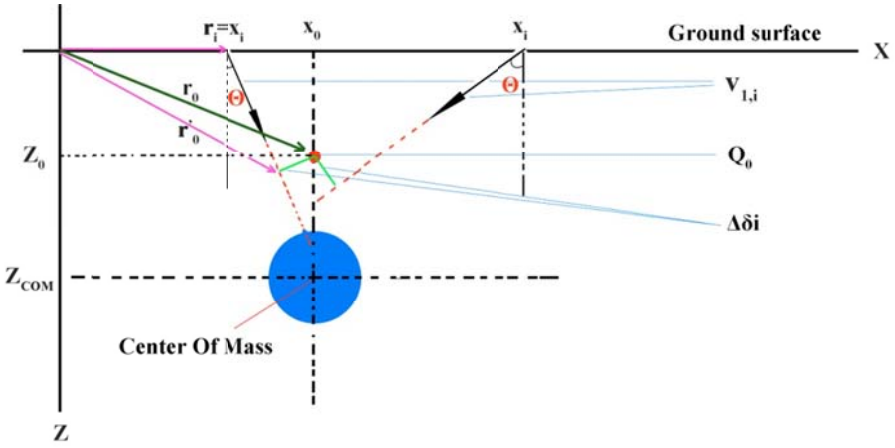

(a)

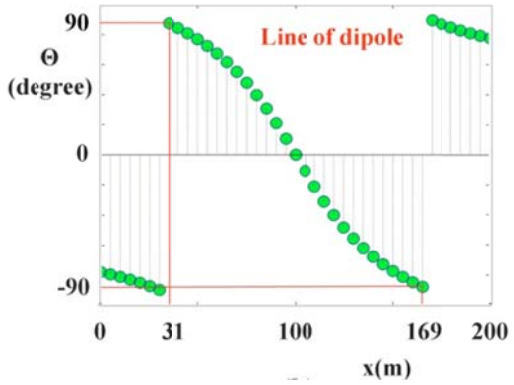

(b)

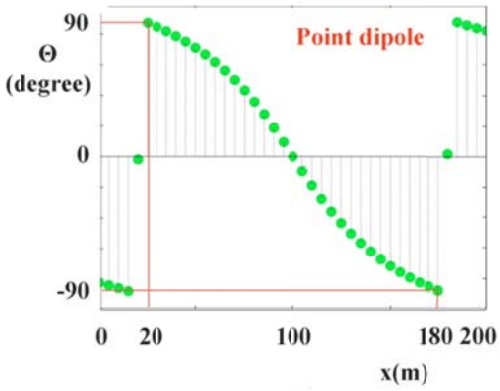

(c)

Figure 1. (a) Schematic profile in $y=y_0$ together with the orientations of first eigenvectors in different locations on the ground in conjunction with the estimated point (Q_0) relating to COM, and COM itself. Θ function in terms of x for (b) A line of dipoles at the point (100 m,100 m,40 m) with an arbitrary profile line where $y=y_0$ (perpendicular to the strike direction); and (c) A point dipole at (100 m, 100 m, 40 m) with a profile line passing over its COM (this profile line is $y=y_0$).

The applied noise is a random Gaussian noise with standard deviation equal to 20 percent of B (measured magnetic fields). To avoid Gibbs phenomenon out of discontinuity of discreet Fourier transform in calculation of RTP field and the derivatives of its components, the data is tapered such that the tapering value is stated as a ratio of three times of the number of data points in half maximum full width of RTP field to the number of total data points in one direction (n=41) (Blakely, 1996). Since we work with

derivatives of RTP magnetic field components, noise disturbs the smoothness of the CMGT component contour maps and first eigenvector directions remarkably. Consequently, we have to moderate these turbulent effects. Firstly, a "moving twenty five point averaging" method is employed. In this method, the average of a magnetic field data point and its twenty four surrounding points in a grid map is calculated and attributed to the main point. By doing this, the disruptive effects of noise are reduced to a great extent. Secondly, the data is continued 5 meters upward. Afterwards, the dimensions of window are changed to give a solution with MSE. The precision of the estimated "COM"s is presented in Table 1. The greater uncertainties in the estimated COM values of horizontal cylinders in comparison with those of spheres are caused by the first eigenvectors, in a square window, which point toward a linear COM, not a single point. The results for all the solitary and binary models are indicated in Table 1. Figure 2 shows the magnetic field, RTP field and six components of CMGT pertaining to cylinder "B" with 20% of noise. Figure 3(d), (e) and (f) indicate B_{zz} map of the three binary systems in the presence of 20% noise. The white and black circles are the real and estimated COMs, respectively.

Table 1. The specification of synthetic isolated and binary models and their solutions together with the characteristic of two sets of real data and their solutions (in the last two rows).

Model		Di* (m)	St* (x,y,z)	In* (°)	De* (°)	RCOM* (m,m,m)	No* (%)	UC* (m)	WS* (length, width)	Tap* (%)	ECOM(m)* (m,m,m)	MSE* (%)
Cylinder (A)		18	(1.0, 0.0,0.0)	-50	30	(100,100,60)	0	0	(90,90)	80	(100±1.4,100±1.7,61.1±2.6)	9.97
							20	5	(90,90)	80	(100.7±1.4,99.7±1.6,67.3±2.8)	8.56
Cylinder (B)		14	(0.7,0.7,0.0)	-70	0	(100,100,40)	0	0	(50,50)	36	(99.9±1.5,100.0±1.5,39.9±2.9)	16.23
							20	5	(70,70)	36	(100.4±1.6 ,100.1±1.6, 37.6±2.7)	14.62
Sphere (A)		10	-	-30	15	(100,100,30)	0	0	(10,10)	37	(100.0±0 ,100.0±0, 29.9±0)	0.14
							20	5	(30,30)	58	(100.5±0.1 ,99.7±0.1, 34.7±0.2)	0.82
Sphere (B)		16	-	-60	45	(100,100,50)	0	0	(10,10)	65	(100.0±0 ,100.0±0, 50.3±0)	0.09
							20	5	(50,50)	80	(100.3±0.1 ,100.7±0.1, 50.9±0.2)	0.55
Binary Cylinders	Cylinder (C)	6	(0.0,1.0,0.0)	-40	0	(100,70,27)	20	5	(30,30)	51	(99.9±1.5 ,69.5±1.7, 23.0±3.3)	25.50
	Cylinder (D)	9	(0.0,1.0,0.0)			(100,130,33)			(40,40)	51	(100.6±1.5 ,130.4±1.7, 35.0±3.4)	18.33
Binary Spheres	Sphere (C)	11	-	-40	0	(70, 70,39)	20	5	(10,10)	65	(70.6±0 ,69.0±0, 43.2±0.4)	1.11
	Sphere (D)	14	-			(130,130,44)			(30,30)	65	(130.2±0 ,130.0±0, 44.0±0.3)	0.79
Binary Spheres	Sphere (E)	10	-	-50	20	(100,100,40)	20	5	(50,50)	68	(99.5±0 ,100.0±0, 43.9±0.3)	0.62
	Sphere (F)					(100,100,50)						
Real Geological models	Pipeline	-	(1.0,0.0,0.0)	52.5	4.5	-	-	0.20	(4,4)	-	(13.89±0.16 ,11.00±0.13, 2.89±0.25)	18.61
	Elura Orebody	-	-	62.5	9.2	-	-	18	(300 , 300)	-	(501±8 ,1083 ±11, 204±14)	21.8

Di**=DiameterDe**=Declination ***UC**=Upward Continuation ***No**=Noise
***St**=strike ***RCOM**=Real Center Of Mass ***WS**=Window Size ***Ta**=Tapering
***In**=Inclination ***ECOM**=Estimated Center Of Mass ***MSE**=Minimum Standard Error

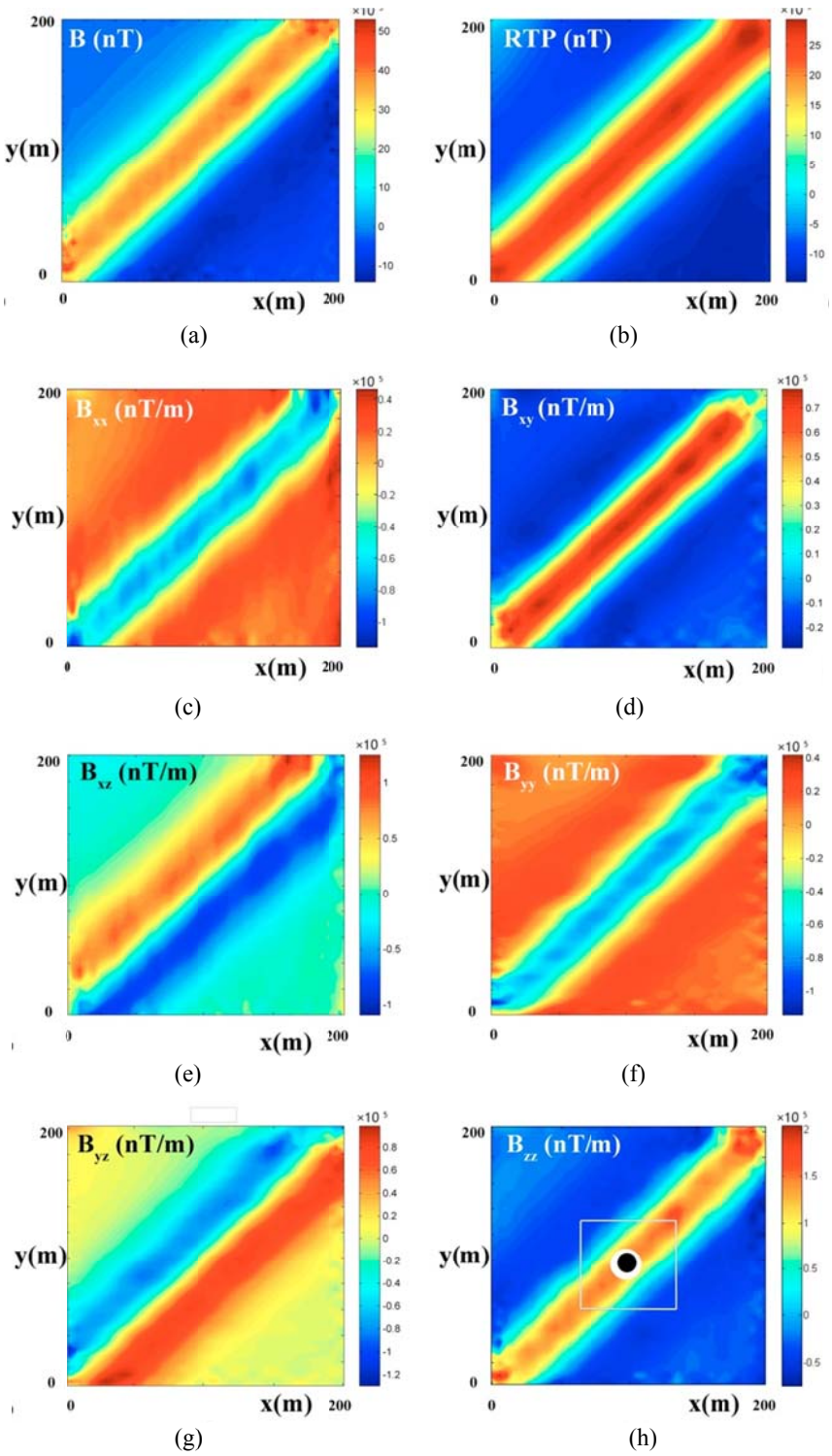

Figure 2. (a) Smoothed main magnetic field (without upward continuation); (b) Smoothed and upward continued RTP field; (c, d, e, f, g, h) Smoothed and upward continued six components of CMGT for cylinder "B" in presence of 20% random Gaussian noise. The area of interest is 205 m×205 m and the cell size is 5 m×5 m. The white and the black circles in (h) are real and estimated COMs, respectively, with the illustrated window giving MSE.

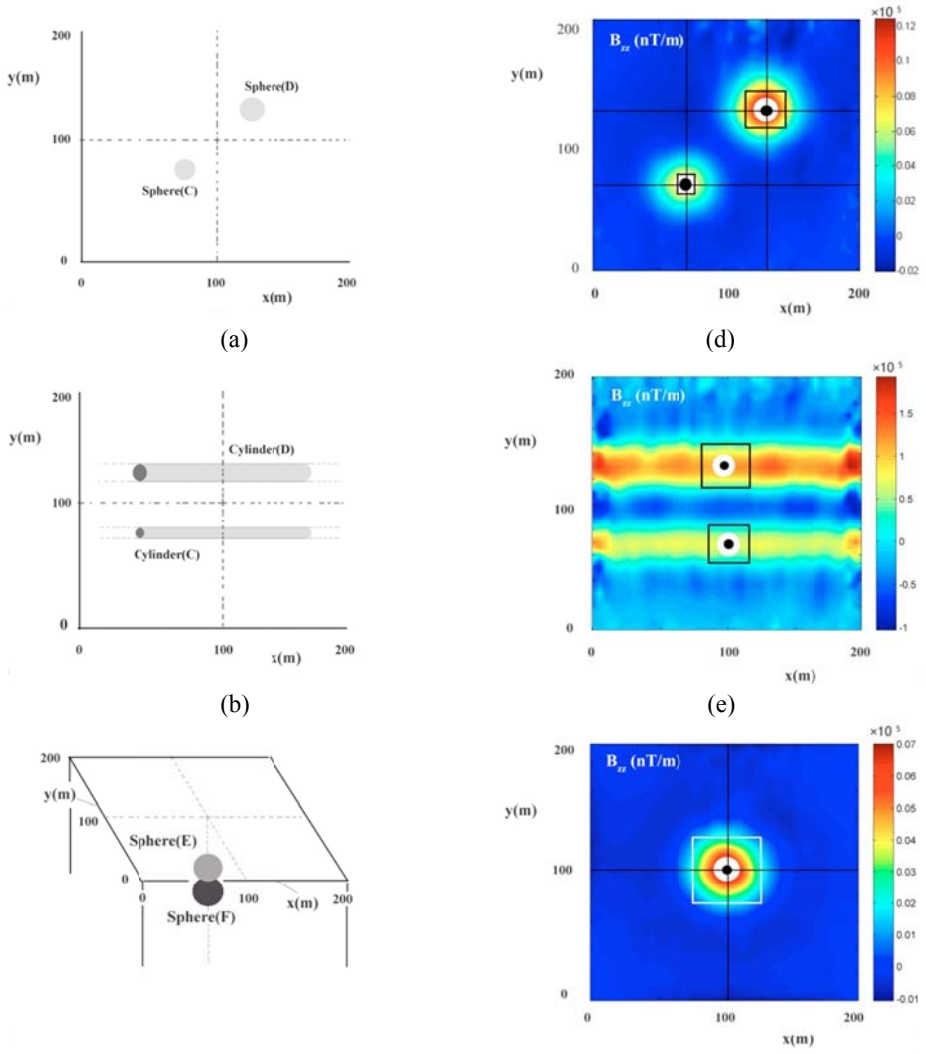

Figure 3. (a) Schematic binary system of spheres in a virtually lateral neighborhood; (b) Schematic binary system of horizontal cylinders in a virtually lateral neighborhood; (c) Schematic binary system of spheres in an absolutely vertical neighborhood; (d, e and f) smoothed and upward continued B_{zz} field of the mentioned binary systems, respectively. The area of interest is 205 m× 205 m and the cell size is 5 m×5 m. The imposed noise on three binary systems is 20%. The black circles in (d), (e) and (f) are the estimated COMs, and the white circles are the true COMs. The windows giving the best results (MSE) are illustrated on each map.

5. Field example

In this section, two real underground examples: 1) an urban gas pipe, and 2) a big spherical mass called "Elura" orebody are analyzed.

5-1. Gas pipe, Kermanshah, Iran

The first real example is a very long buried urban gas pipe around Kermanshah, Iran. The whole area is in sedimentary basin mainly created in Quaternary era. The major formations of the area are arable lands (Q^c), older and younger terraces and gravel fans (Q^{t1} and Q^{t2}, respectively) and alternation of white, yellow, grey, purple, green and red thin bedded Radiolarian bearing mudstone, silisiferous limestone, fossiliferous, neritic and pelagic limestone ($J_3K^r_2$). Since the topography of the area is calm, it has been used for agriculture aims for hundreds of years and no evidence of mineral outcrops has been observed in it. Besides, because the pipe is shallow and the dimensions of the survey area (located in 34° 19' 02" N and 47° 09' 22" E) is very limited (30 m×22 m), it does not comprise any special geological structure (see the circular area in Figure 4). Therefore, all the magnetic field measured at

the study area belongs to the main field as well as the field due to the pipeline. The inclination and declination of total magnetic field are, in turn, 52˚ 30́ and 4˚ 33́. The dimensions of grid map are 30 m×22 m in which the profile length is 30 m. Since the strike direction of this pipe is roughly North-South, the profile directions are almost West-East. The estimated COM by means of our method is (x=13.89±0.16, y=11±0.13, 2.89±0.25), while it was estimated through two methods by Karimi and Shirzaditabar (2017) as (x=14 m, z=2.86 m) and (x=14 m, z=2.94 m). Notice that **y** component of the estimated solution has arbitrary values depending on the window location. Figures 5(a) and 5(b) show the measured total magnetic field and computed B_{zz} map from the smoothed RTP field, respectively. The black circle is the estimated COM and the most suitable window (with MSE) is depicted with dimensions of 4 m×4 m (Figure 5 and Table 1).

5-2. The Elura orebody, New South Wales, Australia

The second geological example is a mine located at the north of the Cobar mineral field of New South Wales in Australia, which is called "Elura" (31˚ 10́ 16.86″ S and 145˚ 39́ 48.91″ E). Mining experience in the Cobar region indicated that the mineralization is stratabound, being hosted in graded siltstones and shales belonging to the Silurian–Lower Devonian CSA siltstone unit of the Cobar supergroup. The geology is concealed beneath about 2 m of regolith, plus up to 10 m of unconsolidated alluvium in drainage depressions; thus, the geology is known mainly from drill holes and pits. A further complication is that the top 0.5 m of bedrock is normally iron stained or ferruginised, and sometimes includes gravels with the magnetic mineral maghaemite (for more study about geology and geological maps of the area, you can refer to Mussett and Aftab Khan (2009)). Using aeromagnetic data, the Elura orebody was modeled as a spherical body with a radius of 118 m and the depth to its center of 250 m (Blackburn, 1980). Ground gravity and magnetic surveys were then carried out over the area in 1973-1974. The pattern of the gravity anomalies suggested that the sphere approximation could be used, and the depth to the center was estimated 194 m. Besides, from the half-width of ground magnetic survey, this depth was estimated as 209 m (Mussett and Aftab Khan, 2009). This study used the ground magnetic data relating to this mass from Mussett and Aftab Khan (2009) and reproduced the magnetic field, and obtained a solution as (501±8, 1083±11, 204.4±14) (see Table 1). In Figures 5(c) and 5(d), B and calculated B_{zz} are indicated.

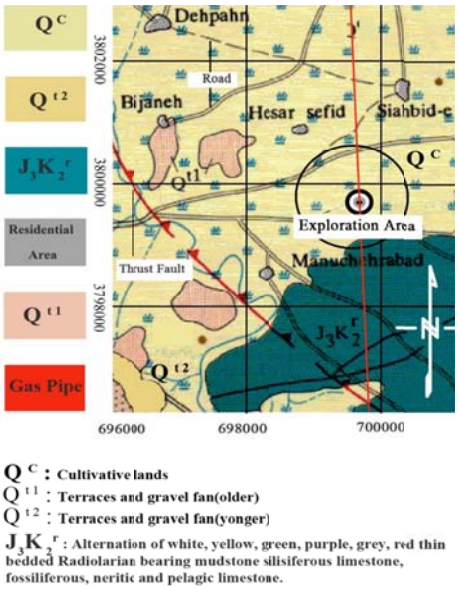

Figure 4. The geological map of gas pipe area. The circle in the central part of the map reveals the area where the data is collected (Karimi Bavandpur and Hajihosseini, 1999). As it is clear, the gas pipe runs approximately from north to south.

6. Conclusion

The applied models in this study were point-dipole and line of dipoles. Because of their magnetic properties, the first eigenvectors of the CMGT do not point toward COM. Nevertheless, in the magnetic poles and in absence of any remanent magnetization, the first eigenvector directions are dependent on the data point locations; only a limited number of them have efficient directions surrounding the body and by moving away from it, they shift away. Using RTP transform and these eigenvectors in the least squares procedure, COM is estimated. The method was tested on a variety of simulated data in absence and presence of noise, as well as two sets of real data. The attained solutions were of acceptable accuracy. After all, as a result of using "twenty-five point averaging" and "upward continuation" techniques, even though we use the derivatives of magnetic field components, noise effects were moderated so much. We hope this method will be developed in source location estimation of some other models like vertical cylinder, dipping dikes or horizontal sheets in future, and predict that the vertical component coefficients for more complex bodies may be related to the ratio between their different dimensions.

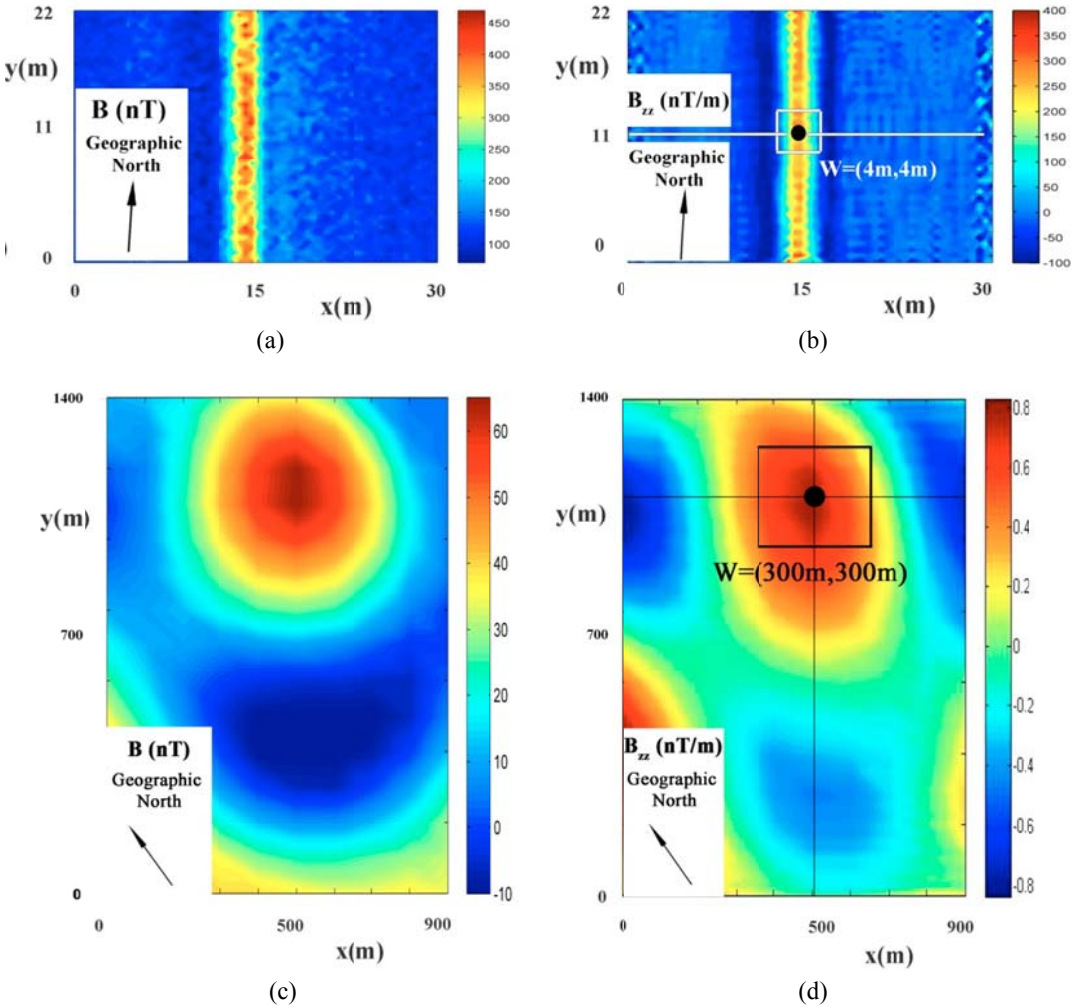

Figure 5. (a & c) measured magnetic fields of the pipe line and Elura orebody (without smoothing and upward continuation), respectively; (b & d) B_{zz} fields, computed from the smoothed and upward continued RTP fields in conjunction with estimated "COM"s (black circles) and the most suitable windows for pipeline and Elura orebody, in turn.

References

Bell, R. E. and Hansen, R. O., 1998, The rise and fall of early oil field technology: The torsion balance gradiometer: The Leading Edge, 17, 81-83.

Beiki, M. and Pedersen, L. B., 2010, Eigenvector analysis of the gravity gradient tensor to locate geologic bodies. Geophysics, 75(6), I37–I49.

Beiki, M., Pedersen, L. B. and Nazi, H., 2011, Interpretation of aeromagnetic data using eigenvector analysis of pseudogravity gradient tensor. Geophysics, 76(3), L1–L10.

Blakely, R. J. and Simpson, R. W., 1986, Approximating edges of source bodies frommagnetic or gravity Anomalies. Geophysics, 51, 1494–1498.

Blakely, R. J., 1996, Potential Theory in Gravity and Magnetic Applications. Cambridge University press.

Blackburn, G., 1980, Gravity and magnetic surveys-Elura Orebody. Bull. Aust. Soc. Explor. Geophys, 11, 59-66

Chianese, D. and Lapenna, V., 2007, Magnetic probability tomography for environmental purposes: test measurements and field applications. J. Geophysics & Engineering, 4, 63-74.

Doll, W. E., Gamey, T. J., Beard, L. P. and Bell, D. T., 2006, Airborne vertical Magnetic gradient for near-surface applications. The Leading Edge, 25, 50–53.

Eppelbaum, L. V., 2015, Quantitative interpretation of magnetic anomalies from bodies approximated by thick bed models in complex environments. Environmental Earth Sciences, 74, 5971-5988.

Frahm, C. P., 1972, Inversion of the magnetic field gradient equation for a magnetic dipole field Naval Coastal Systems. Laboratory Informal Report NCSL, 135–172.

Gamey, T. J., Doll, W. E. and Beard, L. P., 2004, Initial design and testing of a full-tensor airborne SQUID magnetometer for detection of unexploded ordnance. SEG Expanded Abstracts, 23, 798-801.

Karimi Bavandpur, A. and Hajihosseini, A., 1999, 1:100000 geology map of Kermanshah. Geological Survey of Iran publications.

Karimi, K. and Shirzaditabar, F., 2017, Using the ratio of magnetic field to analytic signal of magnetic gradient tensor in determining the position of simple shaped magnetic anomalies. J. Geophysics & Engineering, 14, 769-779.

Mussett, A. E. and Aftab Khan, M., 2009, Looking into the Earth-An introduction to geological geophysics. Cambridge University Press.

Menke, W., 2012, Geophysical Data Analysis Discrete Inverse Theory MATLAB Edition. Academic Press.

Oruc, B., 2010, Location and depth estimation of point-dipole and line of dipoles using analytic signals of the magnetic gradient tensor and magnitude of vector components. J. Appl. Geophys, 70, 27–37.

Pedersen, L. B. and Rasmussen, T. M., 1990, The gradient tensor of potential field anomalies; some implications on data collection and data processing of maps. Geophysics, 55, 1558–1566.

Reford, M. S. and Sumner, J. S., 1964, Aeromagnetics. Geophysics, 29, 482–516.

Reid, A. B., Allsop, J. M., Granser, H., Millet, A. J. and Somerton, I. W., 1990, Interpretation in three dimensions using Euler deconvolution. Geophysics, 55(1), 80–91.

Schmidt, P. W. and Clark, D. A., 2000, Advantages of measuring the magnetic gradient tensor. Preview, 85, 26–30.

Schmidt, D. V. and Bracken, R. E., 2004, Field experiments with the tensor magnetic gradiometer system at Yuma Proving Ground. Arizona Proceedings of the Symposium on the Application of Geophysics to Engineering and Environmental Problems (SAGEEP), February, 2004.

Shaw, R. K., Agarwal, B. N. P. and Nandi, B. K., 2007, Use of Walsh transforms in estimation of depths of idealized sources from total-field magnetic anomalies. Computers and Geosciences, 33, 966–975.